Growth and magnetic properties of vertically aligned epitaxial CoNi nanowires in (Sr, Ba)TiO_3 with diameters in the 1.8–6 nm range

2016 Nanotechnology 27 495601

(http://iopscience.iop.org/0957-4484/27/49/495601)

IOP Publishing Nanotechnology

Nanotechnology **27** (2016) 495601 (10pp) doi:10.1088/0957-4484/27/49/495601

Growth and magnetic properties of vertically aligned epitaxial CoNi nanowires in (Sr, Ba) TiO_3 with diameters in the 1.8–6 nm range

V Schuler[1,6], J Milano[1,2,3], A Coati[4], A Vlad[4], M Sauvage-Simkin[4], Y Garreau[4,5], D Demaille[1], S Hidki[1], A Novikova[4], E Fonda[4], Y Zheng[1,3] and F Vidal[1,3]

[1] Sorbonne Universités, UPMC Univ Paris 06, CNRS-UMR 7588, Institut des NanoSciences de Paris, F-75005, Paris, France
[2] CNEA-CONICET and Instituto Balseiro, UnCuyo. Centro Atómico Bariloche (R8402AGP) San Carlos de Bariloche, RN, Argentina
[3] LIFAN, Laboratoire International Franco-Argentin en Nanosciences, Argentina & France
[4] Synchrotron Soleil, L'Orme des Merisiers Saint-Aubin BP 48, F-91192 Gif-sur-Yvette Cedex, France
[5] Université Paris Diderot, Sorbonne-Paris-Cité, MPQ, UMR 7162, CNRS, Bâtiment Condorcet, Case 7021, F-75205 Paris Cedex 13, France

E-mail: franck.vidal@insp.upmc.fr

Received 15 July 2016, revised 13 October 2016
Accepted for publication 24 October 2016
Published 8 November 2016

Abstract

The growth by pulsed laser deposition of fully epitaxial nanocomposites made of Co_xNi_{1-x} nanowires (NW) vertically self-assembled in $Sr_{0.5}Ba_{0.5}TiO_3/SrTiO_3(001)$ layers is reported. The diameter of the wires can be tuned in the 1.8–6 nm range. The composition of the wires can be controlled, with the growth sequence and the fcc crystallographic structure of the wires preserved for Co content up to 78%. The nanocomposite systems obtained display a uniaxial magnetic anisotropy with out-of-plane easy axis as shown through analysis of ferromagnetic resonance measurements. It is shown that the magnitude of the magnetic anisotropy depends sensitively on the structural quality of the nanocomposites.The energy barrier for magnetization reversal scales as the square of the diameter of the NW and reaches 60 $k_B T_{amb}$ for 6 nm diameter, with $T_{amb} = 300$ K.

Keywords: ferromagnetic nanowires, self-assembly, vertical epitaxy, pulsed laser deposition, ferromagnetic resonance, x-ray diffraction, x-ray absorption

(Some figures may appear in colour only in the online journal)

1. Introduction

In order to overcome the limits of current data storage technologies, the use of three dimensional (3D) spintronic structures has been proposed recently [1, 2]. Such 3D architectures allow one to use out-of-the-plane magnetic domain walls to encode, store and propagate information. This could lead to a huge increase in the density of data storage and to the creation of devices based on novel forms of logic [3–5]. A prerequisite to the successful development of these technologies is the growth of three-dimensional magnetic structures. Ferromagnetic nanowires (NW) represent possible building blocks for such structures. The propagation of magnetic domain walls inside NW has therefore been the subject of intense research during the last years [6–12].

The most commonly used technique to grow ferromagnetic NW is electrodeposition in an alumina template [13–17]. Cobalt–nickel alloy NW grown by this technique have been studied extensively [18–26]. In particular, it has been shown that the possibility to tune the composition of the cobalt–nickel alloy gives a high control over the anisotropy of the

[6] Present address: Institute of Physics ASCR, v.v.i., Cukrovarnická 10, 162 53 Praha 6, Czech Republic.

NW. In this paper, we report on the growth and magnetic properties of cobalt–nickel NW grown using another technique, taking advantage of self-assembly processes occurring during pulsed laser deposition. Such a technique has been used recently to grow systems of metallic wires embedded in an oxide matrix, such as iron NW in a $LaSrFeO_4$ matrix [27], cobalt NW in a yttrium-stabilised zirconia matrix [28], cobalt, nickel and cobalt–nickel NW in a CeO_2 matrix [29–34, 36], and copper nanorods in SrO pillars embedded in a Sr(Ti, Cu)O_3 matrix [37]. The metallic NW grown by sequential pulsed laser deposition exhibit two peculiar features. First, their diameter can be reduced down to 2 nm. Reaching such small values of the diameter has not been possible with electrodeposited NW. Second, a proper choice of the metal/oxide couple may allow one to grow NW in vertical epitaxy within the matrix. As a consequence of the vertical epitaxy, the NW are strained along their axis [36]. This interfacially induced-strain gives rise to a magneto-elastic anisotropy. In the case of nickel NW, the magneto-elastic anisotropy and the shape anisotropy cancel each other [34]. Growing NW made of cobalt–nickel alloys is an efficient way to retrieve an uniaxial anisotropy [34].

In this work, we report the growth of cobalt nickel alloy NW in a (Sr, Ba)TiO_3 (SBTO) matrix by sequential pulsed laser deposition. We also study the influence of the strain field and of the reduced diameter, two specific features of the NWs grown by this technique, on the magnetic properties of the nanocomposite structure.

This paper is organized as follows: in section 2, the experimental details on the growth technique as well as on the structural and magnetic measurements are given; in section 3, the self-assembly of metallic, vertically aligned, NW is evidenced; section 4 concentrates on epitaxy and strain in the nanocomposites; and section 5 focuses on the magnetic properties.

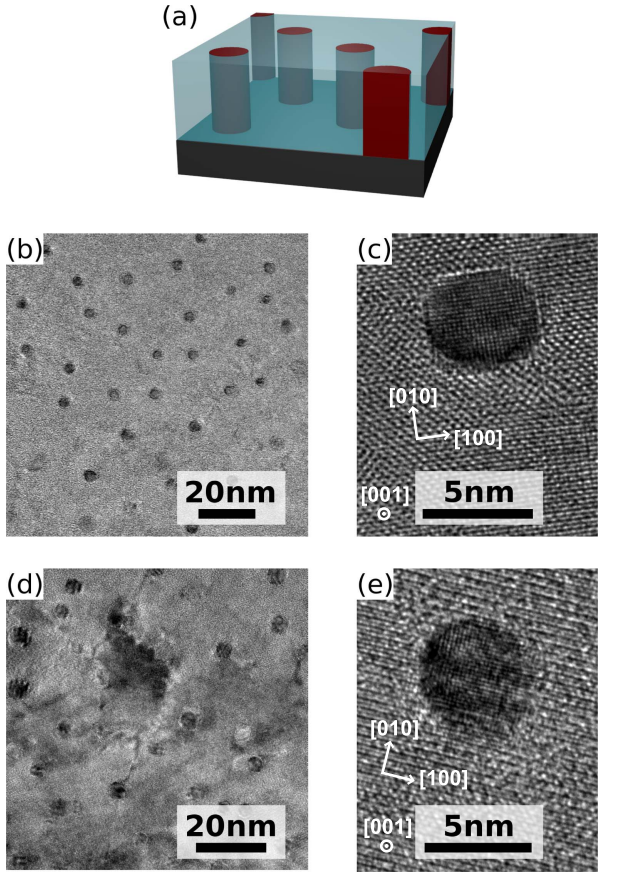

Figure 1. (a) Schematics of the nanowires embedded in the matrix. (b)–(e) TEM plane views of the nanowires: (b) and (c) sample A, (d) and (e) sample B. The crystallographic directions of the matrix are indicated in high-resolution images (c) and (e). [001] is the growth direction.

2. Experimental

The vertical heterostructures were grown by sequential pulsed laser deposition of cobalt, nickel and SBTO on $SrTiO_3$(001) substrates, using a quadrupled Nd:YAG laser (wavelength 266 nm) operating at 10 Hz and a fluence in the 1–3 J cm^{-2} range. The temperature of the substrate during the whole process was 600 °C. First, a 4 nm pure SBTO buffer was grown on the substrate under 0.05 mbar of oxygen. After the buffer growth, the oxygen flux was set to zero and the pressure was lowered below 10^{-5} mbar, with the temperature kept constant. Then, the layer containing the embedded assembly of NW, depicted schematically in figure 1(a), was grown on top of the buffer, by shooting sequentially on NiO, CoO and SBTO targets. The series of shots on the different targets can be described by a single deposition sequence repeated N times. The single deposition sequence can be written as $n_1 \times (n_3 \times \mathrm{CoO} + n_4 \times \mathrm{SBTO}) + n_2 \times (n_3 \times \mathrm{NiO} + n_4 \times \mathrm{SBTO})$, where n_1 is the number of elementary sequences containing the shots on the CoO target, n_2 is the number of elementary sequences containing the shots on the NiO target, n_3 is the number of shots on the NiO or CoO targets and n_4 is the number of shots on the SBTO target. One of the advantages of this sequential deposition is that the composition of the NW can be adjusted by simply changing the ratio n_1/n_2. For example, a deposition sequence with $n_1 = 1$ and $n_2 = 4$ gives NW made of a $Co_{0.2}Ni_{0.8}$ alloy. The ratio n_3/n_4 can be tuned to adjust the diameter and the density of the NW. After the growth, the samples were cooled down to room temperature at a rate of 10 K min^{-1}. Nine samples were grown, labeled from A to I. A is a sample containing NW made of $Co_{0.2}Ni_{0.8}$ embedded in a SBTO matrix, samples B to H contain NW with nominal composition $Co_{0.4}Ni_{0.6}$ and sample I contains NW with nominal composition $Co_{0.8}Ni_{0.2}$. The growth parameters of the samples are listed in table 1.

Transmission electron microscopy (TEM) observation was made using Jeol JEM-2100 LaB6 and JEM-2100F microscopes. The Jeol JEM-2100F microscope is equipped with a field-emission gun operated at 200 kV and a Gatan GIF spectrometer. The samples were thinned using a two-steps procedure including mechanical thinning followed by ion-beam milling in order to reach the required thickness for TEM observation.

Table 1. Parameters of the deposition sequence for the eight samples studied in this article. The series of shots on the different targets during the growth can be described as a single sequence repeated N times. The single sequence can be written as $n_1 \times (n_3 \times \mathrm{CoO} + n_4 \times \mathrm{SBTO}) + n_2 \times (n_3 \times \mathrm{NiO} + n_4 \times \mathrm{SBTO})$.

Sample	n_1	n_2	n_3	n_4	N
A	1	4	1	6	550
B	2	3	5	12	350
C	2	3	6	12	250
D	2	3	4	12	350
E	2	3	3	12	350
F	2	3	3	6	600
G	2	3	3	36	300
H	2	3	1	6	550
I	4	1	1	6	550

Table 2. Diameter, density, axial strain ϵ_{zz}, and composition x of the nanowires, for the samples studied in this article. For samples E and G, the axial strain of the nanowires could not be measured by x-ray diffraction. The composition, x in $Co_xNi_{(1-x)}$, is the nominal one, given by the $n_1/(n_1 + n_2)$ ratio.

Sample	Diameter (nm)	Density (10^{11} cm^{-2})	ϵ_{zz} (%)	x
A	4.4	2.8	0.45	0.2
B	4.9	3.7	1.21	0.4
C	6.0	3.6	1.14	0.4
D	4.8	2.8	1.29	0.4
E	3.6	3.9	—	0.4
F	4.9	6.0	1.32	0.4
G	1.8	8.0	—	0.4
H	3.5	3.0	1.40	0.4
I	3.4	6.0	0.7	0.8

X-ray absorption spectra at the K-edge of cobalt and nickel were measured on the SAMBA beamline at SOLEIL synchrotron (proposal 20120295 and 20130910).

The samples were studied by x-ray diffraction (XRD) measurements at INSP (Rigaku Smartlab diffractometer, Cu Kα radiation) and on the SIXS beamline at SOLEIL synchrotron (proposals 20110234 and 20140220) with a 15.575 keV monochromatic radiation. Studies conducted by synchrotron XRD allowed us to perform detailed reciprocal space mappings. The reciprocal space coordinates (hkl) are defined in the ($a^\star$, $b^\star$, $c^\star$) basis of the reciprocal lattice of cubic $SrTiO_3$ having a lattice parameter equal to 3.905 Å. The surface normal, which is parallel to the growth direction, is oriented along $c^\star$.

The magnetic properties were measured using a vibrating sample magnetometer (VSM) option in a commercial physical properties measurement system (quantum design). A commercial Bruker ESP 300 spectrometer was used for the ferromagnetic resonance (FMR) measurements. The out-of-plane angular variation of the resonance field was measured at a frequency of 24 GHz.

3. Evidence of CoNi NW self-assembly in (Sr, Ba)TiO_3

First, we present the geometrical and chemical properties of the samples grown. Figures 1(b)–(e) show TEM top views of the NW for samples A and B. From the views, the density and the diameter of the NW can be measured. For sample A, the $Co_{0.2}Ni_{0.8}$ NW have a mean diameter of 4.4 nm with a standard deviation of 0.4 nm. The density of the NW is 2.8 10^{11} cm^{-2} which gives a mean distance between NW of about 20 nm. The porosity of the assembly, defined as the ratio of the volume of the NW and the volume of the thin film, is 0.04. For sample B, the $Co_{0.4}Ni_{0.6}$ NW have a mean diameter of 4.9 nm with a standard deviation of 1.4 nm. Their density is 3.7 10^{11} cm^{-2} . In this case, the porosity of the assembly is 0.07. The mean diameter and the density of the NW for the other samples are shown in table 2. Furthermore, the thickness of the deposited film is around 100 nm for all the samples. This ensures that the aspect ratio of the NW is large, with a length over diameter ratio above 20. Finally, XAS shows that the NW are metallic in the samples, with no trace of oxide. The XAS spectra at the K-edges of cobalt and nickel for the sample B are presented figure 2. They are compared to XAS spectra for the metallic and oxide form of cobalt and nickel. These spectra show that both the cobalt and the nickel in the NW are in their metallic form.

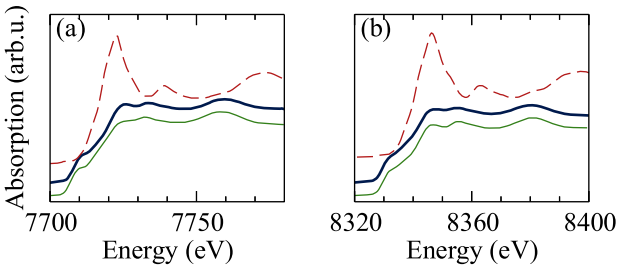

Figure 2. XAS spectra for the sample B at the K-edge of cobalt (a) and nickel (b). In a thick dark blue line, the spectra measured on the sample. In dashed red, the spectrum of CoO (a) or NiO (b). In a thin light green line, the spectrum of a cobalt foil (a) or a nickel foil (b).

In order to check that the composition of the Co_xNi_{1-x} NW follows the nominal one that is controlled through the growth sequence, energy-dispersive x-ray spectroscopy was carried out on TEM samples. We give the spectra for samples A and I in figure 3. These are the two samples at the limits of the composition range tested for the alloy: 20% nominal Co content for sample A and 80% nominal Co content for sample I. Analysis of the spectra (see fits in figure 3) gives the following results for the composition: 16% Co content for sample A and 78% Co content for sample I. This good agreement with the nominal values shows that the composition can effectively be tuned through the growth sequence. The slight deficiency in Co with respect to the nominal composition is ascribed to a small difference in the ablation process efficiency for the CoO and NiO targets during the growth. It should be noted that these measurements average over a large number of wires and that we could not track

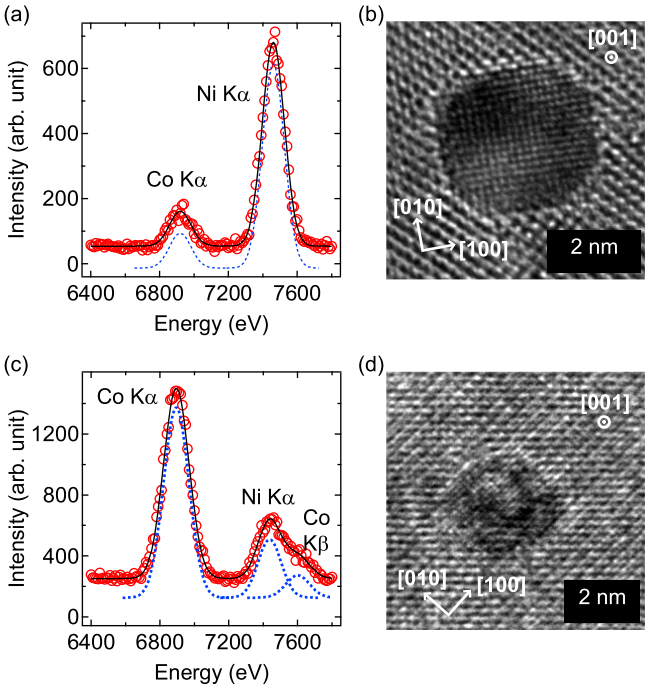

Figure 3. (a) Energy-dispersive x-ray spectrum of sample A in the (Co Kα, Ni Kα) region. Symbols: data, line: fit using two components (one for Co Kα, one for Ni Kα) displayed in dashed line. Adding a weak Co Kβ component did not change significantly the quality of the fit. (b) Representative high-resolution TEM plane view image of a nanowire in sample A. (c) Energy-dispersive x-ray spectrum of sample I. The spectrum was fitted using three components: Co Kα, Ni Kα, and Co Kβ. (d) Representative high-resolution TEM plane view image of a nanowire in sample I.

possible fluctuations of the concentration within single wires due to their very small size.

Having established the metallic character of the NW and discussed their composition, we now turn to their crystalline structure as deduced from local TEM measurements. As shown in figures 1(c), (e) and 3(d), where high-resolution microscopy plane views are displayed, the alloy has a cubic structure. In the bulk, the fcc structure is the most stable one under ambient conditions for Co concentrations below 65% and, beyond this threshold composition, both fcc and hexagonal (hcp) structure coexist [35]. In the present case, close inspection of local TEM images did not reveal any evidences of hcp structure. This could be confirmed by XRD: while peaks related to the fcc structure could be detected, no trace of hcp structure was present.

This shows that the fcc structure is stabilized beyond the Co content threshold existing in the bulk. This is also at variance with previous studies of CoNi NW, of larger diameters than the one studied here, grown in porous alumina templates [24]. In this case, hcp–fcc coexistence was clearly observed in the same composition range than in bulk systems. In the case of the vertically assembled NW under study in the present work, the fcc structure stabilization may find its origin to the epitaxial character of the system, that is discussed in the next section, combined with the reduced diameter of the wires, in the nanoscale range. Energy minimization at the interface between the cubic matrix and the NW should be more efficient in the case of the fcc structure than in the case of the hcp one. Indeed, it should be noted that at the growth temperature (650 °C) the stable phase is the fcc one, irrespective of the Co content. Therefore, for Co content above 65%, the system is likely trapped in the metastable fcc structure during the cooling step following growth as a consequence of interfacial effects that are efficient in the nanoscale regime.

We close this section with a comment on the variations of the density and diameter with the deposition parameters. In the present series of samples, we do not observe a clear law linking the diameter d or the density ρ of the NW to the sequence used for the growth. This is due to the fact that the samples were grown in several growth runs with possible fluctuations of other growth parameters such as the growth temperature, the laser fluence and the background pressure from run to run. Overall, the global trend over the whole set of samples is that ρd^2 increases with the ratio of the number of shots on the transition metal targets over the number of shots on the matrix target.

4. Epitaxy and strain of the nanocomposites

Now, we turn to the study of the crystalline structure of the sample, focusing on the epitaxial character of the system and on the strain in the NW. Every sample of the series was characterized structurally by high resolution TEM in plane-view geometry and XRD at the laboratory ($\theta - 2\theta$ scans). Some of the samples were further studied by synchrotron XRD. We focus here mainly on samples A and B that were thoroughly investigated by reciprocal space mapping.

Figure 4 shows in-plane and out-of-plane XRD measurements as well as reciprocal space mapping around the 202 spot of the substrate for samples A and B. In each measurement, the substrate spot is located at $h = 2$ and/or $l = 2$ exactly, as it serves as a reference to index the reciprocal space. From the matrix spot, we can show that SBTO is cubic and its lattice parameter is 4.01 Å for the two samples A and B. For the other samples, the lattice parameter is between 3.99 and 4.02 Å. These values are greater than what is expected for SBTO, $a_{\mathrm{SBTO}} = 3.955$ Å [38]. A deviation from perfect stoichiometry, due to the low ambient pressure during the growth, can explain the greater lattice parameter [39].

Turning to the diffraction peaks related to Co_xNi_{1-x}, the peaks labeled (3) in the l-scans, figures 4(a) and (b), can be indexed as 002 peaks. The peak labeled (3) in the in plane scan in figure 4(c) can be indexed as 220 and the one in the in plane scan in figure 4(d) as 200. This indicates a cube-on-cube epitaxy of Co_xNi_{1-x} in the matrix. This epitaxy is confirmed by reciprocal space mappings such as the one in figures 4(e) and (f). This confirms local studies by TEM evidencing the same cube-on-cube epitaxy.

However, the reciprocal lattice of Co_xNi_{1-x} exhibits some deviations compared to the reciprocal lattice of a perfect fcc lattice: it is not perfectly cubic and the spots are quite broad. Indeed, in what follows, we show that the NW are strained along their longitudinal axis and relaxed

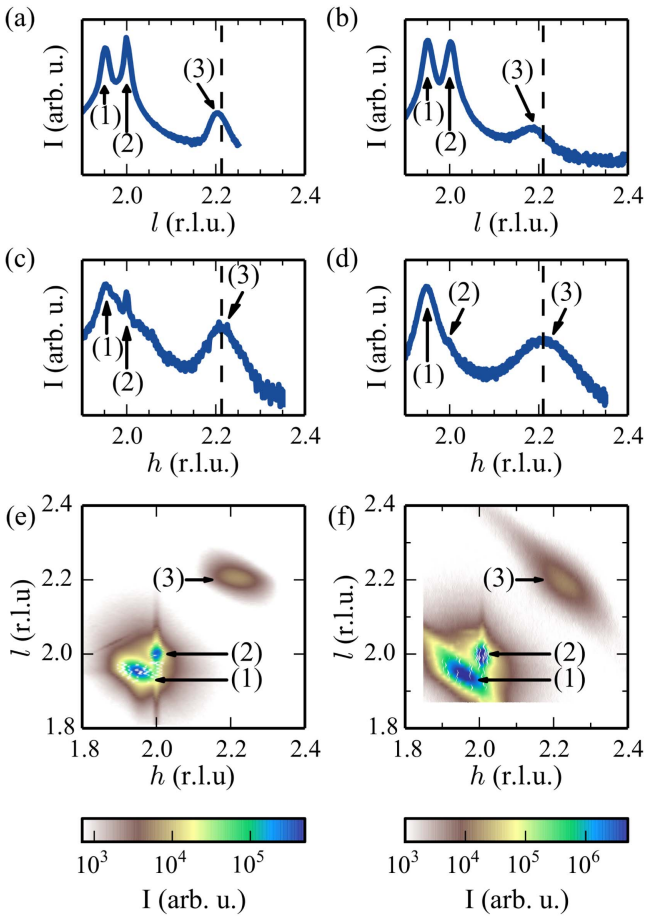

Figure 4. XRD measurements (intensity in log scale) for samples A (a), (c) and (e) and B (b), (d) and (f). (a)–(b) Out-of-plane measurements in specular geometry: *l*-scan at $h = k = 0$, (c)–(d) in-plane measurements, at grazing incidence with l fixed at 0.1: $k = h$ for (c) and $k = 0$ for (d), (e)–(f) reciprocal space mapping around the 202 spot of the substrate. Each peak or spot is labeled by 1, 2 or 3. 1 refers to the matrix, 2 to the substrate and 3 to the nanowires. On figures (a)–(d), the expected peak position calculated from the bulk lattice parameters of the CoNi alloys is shown with a dashed vertical line.

perpendicular to it and that the strain field in the nanowire is inhomogeneous. This axial strain has been reported in other vertically aligned nanocomposites [40] and is a consequence of the vertical interface [36]. The strain state of the wires can be measured by XRD. Indeed in-plane measurements show that the NW are relaxed radially: the in-plane spot is centered on the bulk value marked by a dashed line in the *h*-scans in figures 4(c) and (d). In contrast, the maximum of the 002 spot in the out-of-plane measurements is shifted to the low l values with respect to the bulk value as shown in figures 4(a) and (b). This shows that the NW are in a tensile strain state along the axial direction. The values of the axial strain (ϵ_{zz}) for all the samples are summarized in table 2. For the samples with $Co_{0.4}Ni_{0.6}$ NW, it is greater than 1%. Furthermore, a greater axial strain is obtained for smaller diameters. This has already been shown for nickel NW in ceria [36]. It is a consequence of the increase of the influence of the matrix on the NW [36].

Figures 4(e) and (f) show the mappings around the 202 spot of the substrate. The spots of the substrate, the matrix and the NW can be indexed, confirming the epitaxy of the NW in the matrix. Yet, the spots of the matrix and the NW have a slightly ortho-radial shape for sample B. This suggests that the matrix is slightly textured. Since the NW are epitaxial in the matrix, the axis of the NW should follow the polycrystallinity of the matrix. Therefore, the NW would be slightly misaligned, compared to each other. This could explain the out-of-plane spot of the NW being ortho-radial and is consistent with the observed larger width of the in-plane peak of the substrate for sample B. It is also possible that there is some polycrystallinity inside the NW. In order to disentangle the two effects, we can measure the ortho-radial width of each spot at half height. The matrix spot spans over 0.5° while the NW one spans over 1.5°. Therefore, there is indeed some mis-orientation of the metal lattice with respect to the matrix one. The width of the mis-orientation distribution is of the order of 1°.

To conclude this part, we should point out that the detailed study of the inhomogeneities in the NW and their analysis using reciprocal space mapping is beyond the scope of this paper. Preliminary analysis of the mapping allows us to deduce the coherence length along the [001] direction. In the case of sample A, this length is 14 nm and in the case of sample B, it drops to 8 nm, indicating an increase of the crystalline disorder. From laboratory diffraction measurements, the drop of the coherence length along the [001] direction is common to the NW samples for Co content of 40% and above. To summarize, the NW are strained along their axis, relaxed radially and in sample B there is some texture and disorder, with a characteristic length of 8 nm, in the NW.

5. Magnetic properties of the nanocomposites

The abilty to control the composition of the NW provides the opportunity to study the magnetic anisotropy of these nanostructures. Indeed, there are several sources of magnetic anisotropy in these vertically assembled structures: magnetostatic, magnetocrystalline, and magneto-elastic anisotropy. These different terms depend on the composition of the alloy and the last one depends on the strain. Moreover, the diameter of the objects is in a barely studied range, between 1.8 and 6 nm. This naturally raises the question of the stability of these systems against thermal fluctuations, i.e. the question of the transition towards the superparamagnetic regime at the nanoscale. In what follows, we address these two questions, namely the study of the magnetic anisotropy and the variation of the energy barrier for reversal with the diameter.

5.1. Magnetic anisotropy

Figure 5 shows the in-plane and out-of-plane magnetic hysteresis cycles of samples A and B, measured at $T = 10$ K. In both cases, the cycle obtained when the field is applied along the axis of the wires (out-of-plane) is squarer than the cycle obtained with the field applied in plane. The remanent magnetization and coercive field are much larger when the field is

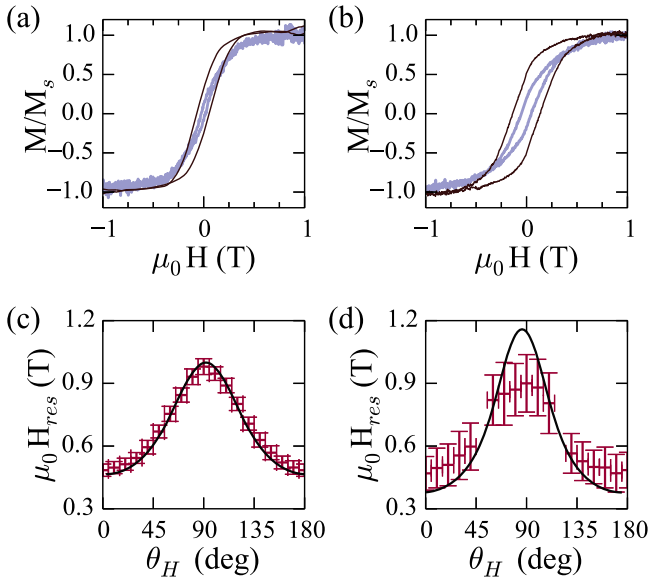

Figure 5. Magnetic measurements on sample A and B. (a) and (b) Magnetic hysteresis cycles measured at $T = 10$ K with a VSM. (a) The measurements on sample A. (b) The measurements on sample B. The cycle in a thick line corresponds to the in-plane direction, the thin black line corresponds to the out-of-plane direction. (c) and (d) Out-of-plane ferromagnetic measurements and analysis at $T = 300$ K. The red crosses show the resonance field measured at room temperature and the thin black lines show the calculated values of resonance field, in the Smit–Beljers formalism, as a function of θ_H (the angle between the normal of the thin film and the static magnetic field applied in the FMR experiments). (c) The data for sample A. (d) The data for sample B.

in the out-of-plane direction which is the easy magnetic axis, as will be shown by FMR measurements. The fact that the cycles are not closed, most notably in the case of sample B, and exhibit rounded shape when the field is applied in the plane can be explained by two effects: (i) the wires are epitaxial with [001] parallel to the growth direction and (ii) the angular misalignment of the wires. Because of (i), the magnetocrystalline anisotropy introduce some local minima in the anisotropy surface along ⟨111⟩ directions and the anisotropy is not purely uniaxial, leading to an increase of the coercive field when the applied field lies in the plane. Moreover, the misalignment of the wires will also induce an increase of the coercive field in the hard direction. These effects, coupled to the shearing effect of the dipolar coupling between wires, lead to the observed in-plane loops.

The coercive field is larger for the $Co_{0.4}Ni_{0.6}$ sample than for the $Co_{0.2}Ni_{0.8}$. This is what one would expect for wires with similar shape and structural quality, since the total magnetic anisotropy is expected to increase when the Co content increases. However, care should be taken when analyzing the variation of the coercive field from sample to sample because it is strongly affected by extrinsic parameters. Indeed, in a study of electro-deposited CoNi wires, it was shown that the coercive field decreased when the Co content increased as a consequence of fcc and hcp phase coexistence in the system [24]. In the present case, we could not derive any clear correlation between the value of the coercive field and the composition over the whole set of samples studied. We attribute this to the very small diameter of the wires and the associated mechanism of magnetization reversal. As the diameter is in the 1.8–6 nm range, it is below the critical diameter for reversal through the nucleation of a transverse domain wall. Such nucleation will proceed at the extremities or at defective portions of the wires and the value of the critical field for nucleation will be very sensitive to the shape. It is thus possible that the degree of faceting of the wires (see e.g. figure 3(b)) will affect the value of the critical field for reversal.

In order to derive quantitative information on the magnetic anisotropy, we have thus performed FMR experiments that will be detailed in what follows. The magnetic cycles can be understood by studying the total magnetic anisotropy of the thin film. There are three contributions to it. First, we address the case of the magnetostatic anisotropy, $F_{\rm ms}$. Since the aspect ratio of the NW is large, the anisotropy is uniaxial and its energy is given by the expression [41]:

$$F_{\rm ms} = \frac{\mu_0 M_S^2}{4}(1 - 3P)\sin^2\theta = K_{\rm ms}\sin^2\theta, \qquad (1)$$

where M_S is the saturation magnetization, P is the porosity of the NW assembly, θ is the angle between the magnetization vector and the normal to the surface, and $K_{\rm ms}$ is the magnetostatic anisotropy constant. Second, the magnetocrystalline anisotropy, $F_{\rm mc}$, which is cubic for $Co_{0.2}Ni_{0.8}$ and $Co_{0.4}Ni_{0.6}$. Third, the magnetoelastic anisotropy which is uniaxial and given by the expression:

$$F_{\rm me} = \frac{3}{2}\lambda_{001}\mu(\epsilon_{zz} - \epsilon_{rr})\sin^2\theta = K_{\rm me}\sin^2\theta, \qquad (2)$$

where λ_{001} is the magnetostriction coefficient of the magnetic material, $\mu = c_{11} - c_{12}$ its shear modulus, ϵ_{zz} the out-of-plane strain and ϵ_{rr} the in-plane strain, which is zero here. The values of the different coefficients and different anisotropy constants for samples A and B are summarized in table 3. These values are given at room-temperature [42–44]. At low temperature, the different anisotropy contributions retain the same order of magnitude in absolute, the only drastic change is a change of the sign of the magnetocrystalline anisotropy for 20% Co content. In both cases, however, the magnetocrystalline anisotropy remains at least two orders of magnitude smaller than the other contributions.

For sample A, the magnetoelastic anisotropy and magnetocrystalline anisotropy constants are negligible, compared to the magnetostatic anisotropy constant. Therefore, for sample A, the magnetostatic anisotropy is the main contribution to the total magnetic anisotropy. It is a uniaxial anisotropy, giving an easy magnetic axis along the axis of the NW. For sample B, the magnetostatic and the magnetoelastic anisotropies are of the same order of magnitude, while the magnetocrystalline anisotropy is negligible. As a consequence, the total anisotropy is a uniaxial anisotropy, giving an easy magnetic axis along the axis of the NW. The hysteresis cycles measurements can be qualitatively explained by considering the total anisotropy in the system. Yet, we cannot extract a quantitative value for the anisotropy from the

Table 3. Coefficient values for the different magnetic anisotropies of the system at room temperature. M_s is the magnetization of the alloy of the nanowires, P is the porosity of the assembly of nanowires. K_{ms} is the magnetostatic anisotropy constant. K_1 is the magnetocrystalline anisotropy constant [42]. λ_{001} is the magnetostriction coefficient of the magnetic material [43], $\mu = \frac{c_{11}-c_{12}}{2}$ its shear modulus [44], ϵ_{zz} the axial strain of the nanowires, K_{me} the magnetoelastic anisotropy constant. The data are given at 300 K.

Sample	M_s (A m^{-1})	P	K_{ms} (J m^{-3})	K_1 (J m^{-3})	λ_{001}	μ (GPa)	ϵ_{zz} (%)	K_{me} (J m^{-3})
A	$6.7\ 10^5$	0.04	$1.23\ 10^5$	$-7\ 10^2$	$1.1\ 10^{-5}$	54	0.45	$8.6\ 10^3$
B	$8.4\ 10^5$	0.07	$1.75\ 10^5$	$-6.8\ 10^3$	$8.2\ 10^{-5}$	51	1.2	$1.2\ 10^5$

coercitive field, as the magnetic reversal in the NW is incoherent.

In order to quantify the different anisotropies at play, out-of-plane FMR measurements were conducted on samples A and B at room temperature (figures 5(b) and (c)). In this part, we show the results and analyze the measurements. The analysis of the FMR measurements was done using the Smit–Beljers formalism, in which the resonance frequency ω_R is calculated as a function of the second derivative of the magnetic free energy F evaluated at the equilibrium angles:

$$\left(\frac{\omega_r}{\gamma}\right)^2 = \frac{1}{M_s^2 \sin^2\theta}\left(\frac{\partial^2 F}{\partial\theta^2}\frac{\partial^2 F}{\partial\phi_M^2}\right) - \frac{1}{M_s^2 \sin^2\theta}\left(\frac{\partial^2 F}{\partial\theta\partial\phi_M}\right)^2, \tag{3}$$

where γ is a constant defined as $\gamma = \frac{g\mu_B}{\hbar}$ (with g the gyromagnetic factor, μ_B the Bohr magneton and $\hbar$ the reduced Planck constant), M_s is the saturation magnetization of the sample, θ is the angle between the normal of the thin film and the magnetization, as defined previously, and ϕ_M is the angle between the [100] direction of the Co_xNi_{1-x} lattice and the in-plane projection of the magnetization. The magnetic free energy used to solve the equation is the sum of four terms:

$$F = F_z + F_{ms} + F_{mc} + F_{me}, \tag{4}$$

where F_z is the Zeeman energy, given by the expression $F_z = -\mu_0 M_s H \cos(\theta - \theta_H)$, with H the amplitude of the static magnetic field, θ_H the angle between H and the normal to the thin film. F_{ms}, F_{me} and F_{mc} are respectively the magnetostatic (equation (1)), magnetoelastic (equation (2)) and the magnetocrystalline anisotropies. The values presented in table 3 were used for the anisotropy constants. As for the low temperature case, the magnetocrystalline anisotropy is negligible for samples A and B, and the magnetoelastic one is also negligible for sample A. For both samples a total uniaxial anisotropy was thus considered and equation (3) was solved for different values of θ_H. The resulting resonance fields were compared directly to the experimental data (see figure 5(c) for sample A and (d) for sample B).

In the case of sample A, composed of $Co_{0.2}Ni_{0.8}$ NWs, the expected resonance fields are in remarkable agreement with the experimental measurements, as shown in figure 5(c). It is indeed possible to reproduce exactly the variation of the resonance field with the expected uniaxial anisotropy ($1.23\ 10^5$ J m^{-3}). This shows that it is possible to grow samples with a purely uniaxial, magnetostatic in origin, anisotropy by adjusting the composition of the Co_xNi_{1-x} alloy.

In the case of sample B, the calculated resonance fields are different from the experimental one, indicating that the total anisotropy of the system is weaker than the expected anisotropy. Indeed we get $1.0\ 10^5$ J m^{-3} instead of $2.95\ 10^5$ J m^{-3}. The enhancement of the anisotropy expected because of the magnetoelastic contribution is not observed. We consider two reasons for the loss of anisotropy in sample B: the misalignment of the NW and the structural or compositional disorder in the NW.

First, from the reciprocal space mapping, we suggested that the NW could be slightly misaligned compared to each other. However this cannot account for the loss of anisotropy in the system. In order to show this, the expression of the magnetostatic anisotropy was modified to take into account a misalignment of the NW. The new expression of its free energy is:

$$F_{ms}^{\star} = \frac{1}{N}\sum_{i=1}^{N}\frac{\mu_0 M_S^2}{4}(1 - 3P)\sin^2(\theta - \theta_{0,i}), \tag{5}$$

where $\theta_{0,i}$ is a normal distribution with a mean value of zero and a standard deviation of 0.5°. When solving the Smit–Beljers equation with this magnetostatic energy, one finds the same resonance fields as the one with the magnetostatic energy from equation (1). Therefore, a simple misalignment among the NW cannot explain the reduced anisotropy.

Second, we have seen that the NW are textured in sample B. Reciprocal space mapping indicates that there is some misalignment of the crystalline axes of the wires, with a width of the order of 1°. Also, the coherence length along the [001] direction is reduced, falling to 8 nm. Thus, there is some crystalline disorder inducing inhomogeneities at the nanoscale. Local fluctuations of λ_{001} and of the strain are likely the source of a strong decrease of the magneto-elastic anisotropy. It should be noted that the same result has been obtained for sample F: textured NW and a reduced total magnetic anisotropy. A reduction of the contribution of the magneto-elastic anisotropy is also present in the case of sample I with 78% Co content. Indeed, taking into account the K_{me} contribution should lead to an anisotropy field of 1.0 T in this case (and 0.65 T when considering solely the magnetostatic anisotropy). Figure 6 shows the magnetic cycles acquired with the field applied along the easy axis and perpendicular to it. Obviously, the saturation field in the hard direction is too small to be consistent with an anisotropy field of 1 T. In the case of this sample, the coherence length is also reduced. This is consistent with the fact that crystalline disorder at the nanoscale has an impact on K_{me}. Finally, local variations of

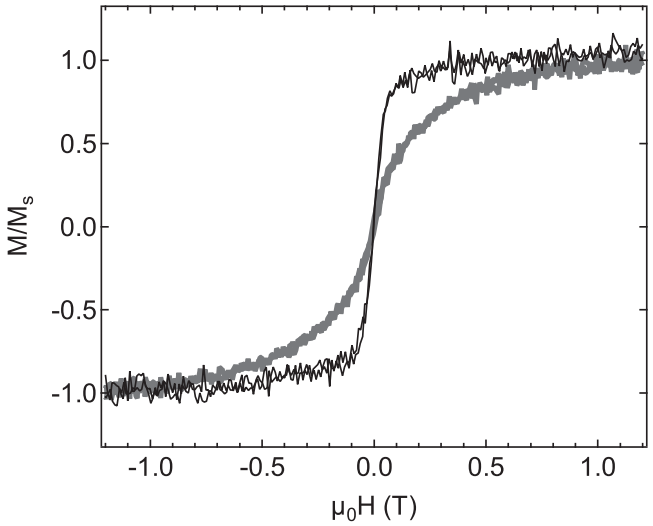

Figure 6. Magnetic hysteresis cycles of sample I measured at $T = 300$ K with a VSM. The cycle in a thick line corresponds to the in-plane direction, the thin black line corresponds to the out-of-plane direction.

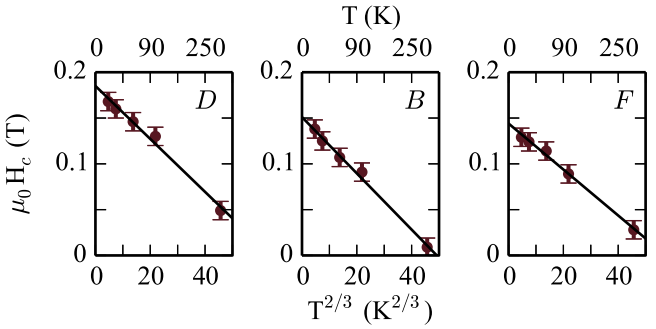

Figure 7. Evolution of the coercive field (symbols) as a function of $T^{2/3}$, where T is the temperature and fit (line) with equation (6) for samples D, B and F. On the upper axes, the corresponding values of temperature are shown. $T_{amb} = 300$ K.

the composition at the nanoscale may also affect the magneto-elastic anisotropy. However, such compositional disorder, if it exists, could not be probed in our TEM measurements.

Before concluding this part, we should note that we expected to increase the total anisotropy of the system through magneto-elastic coupling, taking advantage of the strain induced by the vertical interface. The idea of using the strain to modify and adjust the physical properties in vertical heterostructures has been suggested and demonstrated before [45]. Here, we see that despite the NW being epitaxial in the matrix, the influence of the strain on the magnetic properties is not as high as expected for sample B. Although a detailed study of this point is beyond the scope of the present paper, the loss of anisotropy may be linked to disorder at the nanoscale. Indeed, for sample A, in which no texture of the NW is measured, the measured anisotropy is the expected one. Moreover in the case of strained Ni NW in CeO_2/$SrTiO_3$(001), the effect of the magneto-elastic anisotropy was clearly evidenced through a compensation of K_{ms} and K_{me} (λ_{001} is negative in the case of pure Ni) [34]. Therefore, it may be possible to obtain vertically aligned heterostructures with the expected properties, taking advantage from the fact that λ_{001} is positive for Co_xNi_{1-x} with x above 0.2. In this respect, future work should concentrate on obtaining of CoNi alloys NW with large ϵ_{zz} values and low structural disorder in order to verify experimentally the appealing possibility of enhancing the total anisotropy through magneto-elastic coupling.

5.2. Energy barrier for reversal

Now, we study the influence of the temperature on the stability of the magnetic states of the NW. More precisely, we study the stability of the magnetic states of the NW against thermal fluctuations. Due to thermal fluctuations, the coercivity of a nanostructure can vanish beyond the blocking temperature, and the system enters the superparamagnetic regime. The blocking temperature is directly linked to the energy barrier for magnetization reversal. Obviously, in the perspective of applications, the energy barrier E should be large enough to avoid the superparamagnetic transition at practical temperatures, above room-temperature. E scales as $KV^\star$, where K is the magnetic anisotropy and $V^\star$ is the volume of activation that can be smaller than the actual physical volume of the nanostructure. Thus, controlling the size of the nanostructures can be a way to tailor E. In what follows, we take benefit of our ability to tune the diameter of the NWs in the 1.8–6 nm range in order to explore the variation of E when the size of the NWs varies. We restrict this study to the set of samples going from B to H, having all the same composition ($Co_{0.4}Ni_{0.6}$) and therefore comparable values of magnetostatic anisotropies.

The energy barrier for the magnetic reversal can be determined from measurements of the coercive field as a function of the temperature [46]:

$$H_c(T) = H_{c,0}(1 - (25k_BT/E)^{2/3}), \quad (6)$$

where $H_c(T)$ is the coercive field at temperature T, $H_{c,0}$ is the coercive field for $T = 0$ K, and E is the energy barrier for the magnetic reversal. We measured the coercive fields of samples B to H as a function of the temperature. The data have been adjusted with equation (6). The data and the fit for samples B, D and F are presented figure 7. From the fitting procedure, the energy barrier can be determined for each sample of the series.

Figure 8 shows that the energy barrier for the magnetic reversal increases when the section of the NW increases. In the case of the $Co_{0.4}Ni_{0.6}$ NW, that have high aspect ratio and diameter below 10 nm, the magnetic reversal is incoherent and occurs through nucleation and propagation of a transverse domain wall, with the magnetization inside the domain wall being perpendicular to the wire's longitudinal axis [48]. The energy of the domain wall is given by:

$$E = s\lambda_0\frac{\mu_0 M_S^2}{4} + s\frac{\pi^2 A}{\lambda_0}, \quad (7)$$

where A is the exchange stiffness of the material, s the section of one nanowire and λ_0 the length of the domain wall [47, 48]. For $Co_{0.4}Ni_{0.6}$, $A = 2\ 10^{-11}$ J m^{-1}. The first part of

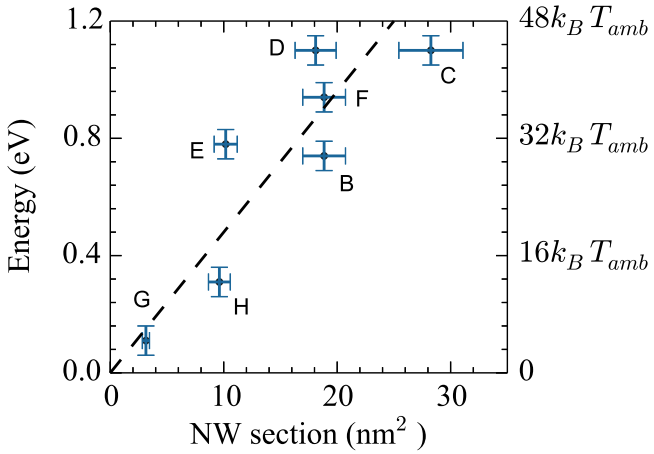

Figure 8. Energy barrier for the magnetic reversal as a function of the section of the nanowires. In blue crosses, the experimental data for samples B to H. Dashed line: energy of a domain wall in a nanowire, given by the equation (7), as a function of the NW section.

this expression is the magnetostatic energy of the domain wall in the nanowire, while the second part is the energy of the domain wall due to the exchange stiffness. This energy is plotted as a function of the section s in figure 8 (dashed line), with $\lambda_0 = 20$ nm. The overall agreement with the experimental points shows that the data are compatible with a magnetic reversal occurring by nucleation and propagation of a 20 nm-long magnetic domain wall. From this model, we find that the barrier of energy for the magnetic reversal of the NW is on the order of $60k_B T_{amb}$ (with $T_{amb} = 300$ K) for NW with diameter of 6 nm. This means that the individual nanowire's magnetization would be stable beyond room temperature in assemblies made of $Co_{0.4}Ni_{0.6}$ NWs with a diameter as low as 6 nm, a diameter falling in the range accessible with the self-assembly growth technique used here.

6. Conclusion

In conclusion, we have reported the growth of nanocomposite structures made of Co_xNi_{1-x} NW vertically aligned in a (Sr, Ba)TiO_3 matrix by sequential pulsed laser deposition. The mean diameter of the NW grown by this technique is adjustable through growth parameters control in the 1.8–6 nm range. The composition of the alloy can be tuned through the sequence used to grow the samples, a fcc structure is observed for Co content up to 78%. The nanocomposite structure is fully epitaxial with cube-on-cube epitaxial relationship. The NW are in tensile strain along their axis, and this axial strain can reach more than 1%.

The evolution of the coercive field with the temperature in the samples is compatible with a model of magnetic reversal including the nucleation and propagation of 20 nm-long magnetic domain wall along the axis of the NW. From this model, we find that a 6 nm diameter is large enough to guarantee an energy barrier of $60k_B T$ for magnetization reversal.

The magnetic anisotropy was studied through FMR measurements. It is shown that a nearly pure uniaxial anisotropy can be achieved in $Co_{0.2}Ni_{0.8}$ wires, as anticipated for this composition of the alloy that leads to negligible contributions of the magnetocrystalline and magnetoelastic anisotropies. In contrast, the possible enhancement of the magnetic anisotropy due to magneto-elastic coupling was not observed for $Co_{0.4}Ni_{0.6}$ wires. This could be correlated with the defective structure of the wires.

In principle, axial strain can be used to increase the magnetic anisotropy in $Co_{0.4}Ni_{0.6}$ NW, through magneto-elastic coupling. Thus, future work on the growth of CoNi alloys NW with large ϵ_{zz} values and low structural disorder is needed in order to achieve the enhancement of the total anisotropy through magneto-elastic coupling in Co_xNi_{1-x}:(Sr, Ba)TiO_3 nanocomposite systems.

Acknowledgments

Synchrotron SOLEIL staff are acknowledged for smoothly running the facility. We thank F Breton for his skillful help and the development of the control software of our PLD apparatus. We thank J-M Guigner, IMPMC, CNRS-UPMC, for access to the TEM facilities. This work has been supported by ANR, grant ANR-2011-BS04-007-01. We thank the LIFAN for funding the sojourn of V Schuler at CNEA-CONICET in San Carlos de Bariloche. J Milano acknowledges Mairie de Paris for the awarded fellowship during his stay at INSP in Paris.

References

[1] Parkin S S, Hayashi M and Thomas L 2008 *Science* **320** 190
[2] Lavrijsen R, Lee J-H, Fernández-Pacheco A, Petit D C M C, Mansell R and Cowburn R P 2013 *Nature* **493** 647
[3] Allwood D A, Xiong G, Faulkner C C, Atkinson D, Petit D and Cowburn R P 2005 *Science* **309** 1688
[4] Currivan J A, Jang Y, Mascaro M D, Baldo M A and Ross C A 2012 *IEEE Magn. Lett.* **3** 3000104
[5] Parkin S S P and Yang S H 2015 *Nat. Nanotechnol.* **10** 195
[6] Wegrowe J E, Kelly D, Truong T, Guittienne P and Ansermet J-P 2001 *Europhys. Lett.* **56** 748
[7] Da Col S *et al* 2014 *Phys. Rev.* B **89** 180405
[8] Koyama T *et al* 2011 *Nat. Mater.* **10** 194
[9] Lei N *et al* 2013 *Nat. Commun.* **4** 1378
[10] Bauer U, Emori S and Beach S D 2013 *Nat. Nanotechnol.* **8** 411
[11] Yan P, Wang X S and Wang X R 2011 *Phys. Rev. Lett.* **107** 177207
[12] Vernier N, Allwood D A, Atkinson D, Cooke M D and Cowburn R P 2004 *Europhys. Lett.* **65** 526
[13] Kawai S and Ueda R 1975 *J. Electrochem. Soc.* **122** 32
[14] Masuda H and Fukuda K 1995 *Science* **268** 1466
[15] Fert A and Piraux L 1999 *J. Magn. Magn. Mater.* **200** 338
[16] Da Col S, Darques M, Fruchart O and Cagnon L 2011 *Appl. Phys. Lett.* **98** 112501
[17] Piraux L, Renard K, Guillemet R, Mátéfi-Tempfli S, Mátéfi-Tempfli M, Antohe V A, Fusil S, Bouzehouane K and Cros V 2007 *Nano Lett.* **7** 2563

[18] Zhu H, Yang S, Ni G, Yu D and Du Y 2001 *Scr. Mater.* **44** 2291
[19] García J, Vega V, Iglesias L, Prida V M, Hernando B, Barriga-Castro E D, Mendoza-Reséndez R, Luna C, Görlitz D and Nielsch K 2014 *Phys. Stat. Sol.* A **211** 1041
[20] Prida V M, García J, Iglesias L, Vega V, Görlitz D, Nielsch K, Barriga-Castro E D, Mendoza-Reséndez R, Ponce A and Luna C 2013 *Nanoscale Res. Lett.* **8** 17
[21] Rosa W O, Vivas L G, Pirota K R, Asenjo A and Vázquez M 2012 *J. Magn. Magn. Mater.* **324** 3679
[22] Pereira A, Gallardo C, Espejo A P, Briones J, Vivas L G, Vázquez M, Denardin J C and Escrig J 2013 *J. Nanopart. Res.* **15** 2041
[23] Talapatra S, Tang X, Padi M, Kim T, Vajtai R, Sastry G V S, Shima M, Deevi S C and Ajayan P M 2009 *J. Mat. Sci.* **44** 2271
[24] Vega V, Böhnert T, Martens S, Waleczek M, Montero-Moreno J M, Görlitz D, Prida V M and Nielsch K 2012 *Nanotechnology* **23** 465709
[25] Vivas L G, Vazquez M, Escrig J, Allende S, Altbir D, Leitao D C and Araujo J P 2012 *Phys. Rev.* B **85** 035439
[26] Xu J and Xu Y 2007 *Appl. Surf. Sci.* **253** 7203
[27] Mohaddes-Ardabili L *et al* 2004 *Nat. Mater.* **3** 533
[28] Shin J, Goyal A, Cantoni C, Sinclair J W and Thompson J R 2012 *Nanotechnology* **23** 155602
[29] Vidal F, Zheng Y, Milano J, Demaille D, Schio P, Fonda E and Vodungbo B 2009 *Appl. Phys. Lett.* **95** 152510
[30] Schio P, Vidal F, Zheng Y, Milano J, Fonda E, Demaille D, Vodungbo B, Varalda J, de Oliveira A J A and Etgens V H 2010 *Phys. Rev.* B **82** 094436
[31] Vidal F, Zheng Y, Schio P, Bonilla F J, Barturen M, Milano J, Demaille D, Fonda E, de Oliveira A J A and Etgens V H 2012 *Phys. Rev. Lett.* **109** 117205
[32] Vidal F, Schio P, Keller N, Zheng Y, Demaille D, Bonilla F J, Milano J and de Oliveira A J A 2012 *Physica* B **407** 3070
[33] Schio P, Bonilla F J, Zheng Y, Demaille D, Milano J, de Oliveira A J A and Vidal F 2013 *J. Phys.: Condens. Matter.* **25** 056002
[34] Bonilla F J *et al* 2013 *ACS Nano* **7** 4022
[35] Hansen M and Anderko K 1958 *Constitution of Binary Alloys* (New York: McGraw-Hill)
[36] Schuler V *et al* 2015 *Nano Res.* **8** 1964
[37] Kim D H, Sun X Y, Aimon N M, Kim J J, Campion M J, Tuller H L, Kornblum L, Walker F J, Ahn C H and Ross C A 2015 *Adv. Func. Mater.* **25** 3091
[38] Terai K, Lippmaa M, Ahmet P, Chikyow T, Fujii T, Koinuma H and Kawasaki M 2002 *Appl. Phys. Lett.* **80** 4437
[39] Tseng T-F, Yeh M-H, Liu K-S and Lin I-N 1996 *J. Appl. Phys.* **80** 4984
[40] Zhang W, Chen A, Bi Z, Jia Q, MacManus-Driscoll J L and Wang H 2014 *Curr. Opin. Solid State Mater.* **18** 618
[41] Encinas-Oropesa A, Demand M, Piraux L, Huynen I and Ebels U 2001 *Phys. Rev.* B **63** 104415
[42] Kadowaki S and Takahashi M 1975 *J. Phys. Soc. Japan* **38** 1612
[43] Kadowaki S and Takahashi M 1981 *J. Phys. Soc. Japan* **50** 1154
[44] Leamy H J and Warlimont H 1970 *Phys. Stat. Sol. B* **37** 523
[45] Zhang W, Jian J, Chen A, Jiao L, Khatkhatay F, Li L, Chu F, Jia Q, MacManus-Driscoll J L and Wang H 2014 *Appl. Phys. Lett.* **104** 062402
[46] Skomski R, Zeng H, Zheng M and Sellmyer D J 2000 *Phys. Rev.* B **62** 3900
[47] Forster H, Schref T, Suess D, Scholz W, Tsiantos V, Dittrich R and Fidler J 2002 *J. Appl. Phys.* **91** 6914
[48] Jamet S, Rougemaille N, Toussaint J C and Fruchart O 2015 *Magnetic Nano- and Microwires, Design, Synthesis, Properties and Applications* ed M Vazquez 1st (Cambridge: Woodhead Publishing)